WILEY-VCH

DOI: 10.1002/ adfm.201502653

Article type: Full Paper

Harnessing Structure-Property Relationships for Poly(alkyl thiophene)-Fullerene Derivative Thin Films to Optimize Performance in Photovoltaic Devices

*Nabankur Deb, Bohao Li, Maximilian Skoda, Sarah Rogers, Yan Sun, Xiong Gong, Alamgir Karim, Bobby Sumpter and David G Bucknall**

[*]Mr. N. Deb, Prof. D. G. Bucknall
School of Materials Science and Engineering
Center for Organic Photonics and Electronics (COPE)
Georgia Institute of Technology, Atlanta, Georgia 30332 (USA)
Email: bucknall@gatech.edu

Mr B. Li, Ms Y. Sun, Prof. X. Gong, Prof A. Karim
Department of Polymer Engineering,
University of Akron, Akron, Ohio 44325 (USA)

Dr. M. Skoda, Dr. S. Rogers
Rutherford Appleton Laboratory,
Harwell Oxford, Didcot, OX11 0QX (UK)

Dr. B. G. Sumpter
Center for Nanophase Materials Sciences and Computer Science & Mathematics Division,
Oak Ridge National Laboratory, Oak Ridge, Tennessee 37831 (USA)

Keywords: polyalkylthiophenes, fullerenes, morphology, bulk heterojunctions, organic photovoltaics

Abstract

Nanoscale bulk heterojunction (BHJ) systems, consisting of fullerenes dispersed in conjugated polymers as the active component, have been actively studied over the last decades in order to produce high performance organic photovoltaics (OPVs). A significant role in device efficiency is played by the active layer morphology, but despite considerable study, a full understanding of the exact role that morphology plays and therefore a definitive method to produce and control an ideal morphology is lacking. In order to understand the BHJ phase behavior and associated morphology in these devices, we have used neutron reflection, together with grazing incidence X-ray and neutron scattering and X-ray photoelectron spectroscopy (XPS) to determine the morphology of the BHJ active layer in functional

devices. We have studied nine model BHJ systems based on mixtures of three poly(3-alkyl thiophenes, P3AT) (A=butyl, hexyl, octyl) blended with three different fullerene derivatives, which provides variations in crystallinity and miscibility within the BHJ composite. In studying properties of functional devices, we show a direct correlation between the observed morphology within the BHJ layer and the device performance metrics, i.e., the short-circuit current (J_{SC}), fill factor (*FF*), open-circuit voltage (V_{OC}) and overall power conversion efficiency (PCE). Using these model systems, the effect of typical thermal annealing processes on the BHJ morphology through the film thickness as a function of the polythiophene-fullerene mixtures and different electron transport layer interfaces has been determined. It is shown that fullerene enrichment occurs at both the electrode interfaces after annealing. The degree of fullerene enrichment is found to strongly correlate with J_{SC} and to a lesser degree with FF. Based on these findings we demonstrate that by deliberately adding a fullerene layer at the electron transport layer interface, J_{SC} can be increased by up to 20%, resulting in an overall increase in PCE of 5%.

1. Introduction

The demand for energy by mankind is rapidly growing, and estimates indicate that current levels of consumption could double to approximately 30 terawatts by 2050.[1] It is also clear that the current fossil-fuel dominated energy system will not meet the demands in the future, requiring us to seek alternative, and crucially, renewable sources. The potential for solar energy to provide a green, renewable energy source has been well understood for many years. The 2011 report by the International Energy Agency found that solar energy technologies such as photovoltaic, solar hot water and concentrated solar power could provide a third of the world's energy by 2060.[2] To date however, the uptake in solar energy technologies is very modest and only accounts for a small fraction of the current energy needs. The need for

cheaper and much more efficient solar energy devices is therefore required if these energy needs are to be addressed in the foreseeable future.

Solar energy devices can be made of organic, inorganic or composite based materials. Organic photovolatics (OPVs) offer the potential for cheaply produced, flexible large area panels. The best performing single-junction polymer based solar cells currently available is over 10%[3] and multi-junction is 11.1%[4]and has come a long way from devices with ~5% efficiencies just a few years ago.[5] However, even the best OPVs have device efficiencies that are significantly below those of inorganic based devices - 29.1% for the best single junction GaAs based cells and 44.1% for a multijunction device made by Sharp[6] - and despite significant research and technological development OPVs still do not offer a plausible option to satisfy household energy requirements. To date, OPVs have been largely developed in two forms, i.e., the bilayer, and the bulk heterojunction structure. The bilayer, made up of two layers of an acceptor material, i.e., a fullerene and the donor polymer, was made for the first time by evaporating a thin layer of C_{60} on top of a spin coated poly[2-methoxy-5-(2'-ethylhexyloxy)-p-phenylene vinylene] layer[7]. The most efficient form of organic based solar devices to date, consist of donor and acceptor materials mixed together to form what is known as a bulk heterojunction (BHJ). The poly(3-hexylthiophene) (P3HT) and [6,6]-phenyl-C_{61} butyric acid methyl ester ($PC_{61}BM$) donor-accepter combination is one of the most widely studied BHJ systems,[8, 9, 10, 11] although more efficient materials have been subsequently appeared in the literature. Even for systems with ideal electronic energy levels, the operating mechanism of OPVs is highly dependent on the nanoscale morphology of the electron donor and the electron acceptor materials. Upon illumination, excitons (bound electron-hole pairs) formed by the photoconductive polymers, which are the source of charge generation, diffuse to the acceptor-donor interface, where excitons dissociate into positive and negative charges that subsequently travel to the respective electrodes to be collected and develop an electric

potential. The exciton diffusion length of ~10 nm thus necessitates the presence of a morphology that is consistent with these length scales. It is thus believed that the active layer ideally consists of interpenetrating domain networks of the acceptor and donor phases [12, 13] The efficiency of OPVs has been seen to depend upon a number of factors such as material choice, processing solvent, interfacial effects, thermal processing and annealing conditions. These factors consequently have a direct effect on the morphology of the systems. A better understanding of these effects and their combined implications, would allow us to fully understand structure-property relationships needed to develop more efficient devices in the future.

It is known that the interaction between the polymers and fullerene derivatives and as well as with the common solvent used in the preparation of the BHJ is critical in determining the morphology of BHJ system.[8, 14] Most of early studies mainly focused on different systems with variations in polymer/fullerene ratio or any chemical changes of one of the species (e.g., side chain of the polymer).[10, 15] However these studies were conducted whilst considering the active layer morphology as an ideal heterogeneous blend throughout the layer. More recent studies have clearly shown that this picture of the active layer morphology is highly naive. They have also shown that a bilayer can be effectively converted into a BHJ through interdiffusion of $PC_{61}BM$ into P3HT by annealing at 150 °C. [16, 17] Earlier studies showed that annealing of the devices has a considerable effect,[5] with both the effects of recrystallization of the polymer and diffusion of the fullerene occurring through the remaining amorphous regions of the polymer having different implications on the device characteristics. [16, 18, 19] [20]

Since the BHJ layers are thin films (of order of 100 nm), the interfacial properties with the bounding electrodes play a significant role in affecting both the morphology and consequently the performance of devices. The morphology that develops in BHJ layer is thus not uniform throughout the thickness of the film, and the effect of such morphological changes on the

device performance is not fully understood. Studies on BHJ systems using a number of different techniques (including NEXAFS [21, 22] and TEM[23]) have observed the segregation of $PC_{61}BM$ through the thickness of the active layer. In the present study we used neutron reflectometry (NR) and X-ray photoelectron spectroscopy (XPS) in order to obtain a depth profile with nanoscale resolution and to quantify interfacial segregation. Other groups have conducted work on BHJ devices using neutron reflectivity. However they have been performed, either in the absence of the top electrode [24] or have only studied just one particular system (P3HT:$PC_{61}BM$).[25, 26] Studies such as these and ones with other semicrystalline polymer: fullerene systems,[27] have however shown that with NR it is possible to understand not only the bulk behavior, but also the morphological evolution at the interfaces and subsequently the entire device structure. The same study subsequently identified the presence of a polymer enrichment layer at both the top and bottom electrode with the bulk of the active layer having a constant ratio of the polymer and fullerene in both as cast and annealed films. Annealing led to an enrichment of fullerene at the top electrode (aluminum, as is the case in the conventional OPV geometry), which was consequently linked to improved device performance. The presence of the top electrode is also seen to be crucial in the studies of these systems, as it has been seen that preparation and subsequent annealing of devices before and after placing the top electrode give sufficiently different interfacial structure and roughness, resulting in differing device performances. Devices annealed after the deposition of all the composite layers (including the electrode) produced greater roughness at the BHJ/electrode interface providing additional absorption of light. At the same time, greater vertical segregation through the thickness upon annealing is also seen to give better voltage output because of reduced shunt paths and optimal domains of P3HT:$PC_{61}BM$ formed.[28]

Besides the vertical segregation behavior, the in-plane morphology is also important as it has a direct impact on charge separation and transport. Using grazing incidence wide angle scattering (GIWAXS),the crystallinity in the device has been shown to be dependent on a number of factors including the regioregularity,[29] solvent used,[30] its concentration[31] and post processing techniques such as thermal[32] and solvent annealing.[33] To study larger scale morphology in OPV systems small angle scattering using X-rays (SAXS) and neutron scattering (SANS) are both useful. Neutron scattering is particularly powerful due to the natural contrast between the carbon-rich fullerene and the conjugated polymers. In addition, since neutrons are highly penetrating, they also potentially allow the study of the BHJ layer buried below the top electrodes thus managing to keep the BHJs in full device architecture. A number of studies using SANS have been carried out to explore the large scale phase morphology (1-100 nm) in the BHJ blends.[18, 22, 34, 35] However, since these studies were performed in transmission no depth dependent morphology was obtained. Using grazing incidence small angle X-ray scattering (GISAXS) measurements to determine in-plane morphology the absence[22] or presence[34, 35] of PCBM aggregation have been observed in the BHJ layer depending on the materials and processing approaches used.

Through such morphological studies, it is clear that a combination of factors determines the overall morphology and consequently the device performance. To obtain further insight into these factors, we have combined a number of techniques to study the through-thickness morphology (using neutron reflectivity and XPS)) and lateral (in-plane) morphology (using GIWAXS and GISANS) of the bulk heterojunctions in full device architectures. In order to understand the effect of the chemical structure and interaction behavior on the morphology of the heterojunction, we chose BHJ systems consisting of homologous series of three modified fullerenes and three poly(alkyl thiophenes) (P3AT) taken in all possible (nine) binary combinations.

Both the morphological and device measurements were made in full device configuration as shown in **Figure 1** (see Experimental section), and furthermore, both with and without a calcium (Ca) electron transport layer. The Ca not only affects the work function of the electrode, but due to differences in surface energies, also affects the interaction with the BHJ. Devices without Ca were studied both without annealing (i.e., 'unannealed') and also annealed after all the layers were deposited (i.e., 'post-annealed'). Devices with Ca were instead studied when annealed before Ca and Al layers were deposited (i.e., 'pre-annealed') since post-annealing was found to cause electrode oxidation [36, 37] and significantly degrade device performance.

Neutrons are an ideal source for these studies to provide a composition depth profile within the BHJ layer owing to the large neutron scattering length density contrast between the fullerene and P3AT. This led to our choice of neutron reflectivity (NR) and grazing incidence small angle neutron scattering (GISANS) as key characterization techniques. In addition, since neutrons are highly penetrating, we are able to easily study the BHJ layer buried below the top electrodes thus managing to keep the BHJs in full device architecture.

2. Results

2.1 Device Characteristics

Poly(3-alkyl thiophene) (P3AT):fullerene based BHJ devices (ratio 1:1), shown schematically in Figure 1, were prepared as discussed in the Experimental section and the dark and light current-voltage statistics were measured. Devices were measured under both pre- and post-annealing conditions prior to Ca/Al or Al electrode deposition (See Experimental section). As seen in Tables S3 and S4, devices without the Ca layer performed better with annealing post Al layer deposition (post-anneal), whereas devices with the Ca-add layer performed better with only pre-annealing before the Ca/Al deposition (pre-anneal), and these devices were used for further morphological studies using the characterization techniques mentioned earlier.

From the J-V curves shown in Figure S2 the J_{sc}, V_{oc} and the *FF* were extracted for different devices and reported in Tables S3 and S4. For the devices made with and without the Ca add layer, a larger V_{OC} is observed for BHJ containing bis-$PC_{61}BM$ than its counterparts with $PC_{61}BM$, which have larger V_{OC} than C_{60}, which is in good agreement with other reports.[7, 38] On comparing devices made with the same fullerene electron acceptor, the J_{sc} values followed the trend of J_{sc} (P3HT) > J_{sc} (P3BT) ~ J_{sc} (P3OT), i.e., P3HT based devices best facilitate charge transport towards the electrodes. The *FF* of the devices was maximum for the case of P3HT (P3HT>P3OT>P3BT) with any fullerene, and similarly for any polymer the trend observed was $PC_{61}BM$>bis $PC_{61}BM$>C_{60}. The presence of the Ca add-layer produced higher *FF* values in almost all systems compared to Al only devices, the exceptions being for two of the C_{60} containing devices. From the J_{sc}, V_{oc} and *FF* values the device power conversion efficiency (*PCE*), was calculated from $PCE = (V_{oc}*Jsc*FF)/I_o$, where I_o is the incident light intensity. The values obtained are given in Tables S3 and S4 and shown plotted against the number of carbons in the P3AT alkyl side chain in **Figure 2** a. It is seen that devices containing P3HT:$PC_{61}BM$ as the BHJ gave the best device efficiencies among all the P3AT:$PC_{61}BM$ based devices, as has been well known in literature.[39, 40] Interestingly, on post-annealing, the devices showed some improvement in the performance when there is no Ca add-layer, whereas the devices made with Ca showed no improvement, or even an reduction in the PCE, even in the case of P3HT:$PC_{61}BM$. This could be associated with Ca diffusion into the active layer or oxidation of the electrode on annealing after the deposition, leading to a reduction in the short circuit current. [36, 37]

2.2 Density Functional Theory simulations and UV-vis measurements

DFT simulations were carried out on the combination of the nine different oligo(alkylthiophenes)-fullerene pairs (and the complementary interactions: fullerene-fullerene, alkylthiophene-alkylthiophene) to obtain binding energy values. These were further

used to determine the miscibility of the fullerene in the polymer for each system (see Experimental section). It was observed that the binding energy, E_b, decreased with increasing side chain length of poly(3-alkylthiophenes) (Figure 2b), with the highest E_b value for the P3BT:bis $PC_{61}BM$ combination. The trend in caluclated solubility of the fullerenes in each of the polyalkylthiophenes follows the trend bis-$PC_{61}BM$>$PC_{61}BM$>C_{60}. This trend however does not follow the observed trends for experimental macroscopic device properties *Jsc*, *FF*, or *Voc* (although there is good agreement to *Voc*). To probe this behavior, UV-vis absorption measurements were carried out on thin films made of these P3AT-fullerene combinations (see Figure S13). In general the absorption behavior would be expected to correlate with the amount of the sunlight being harnessed and consequently have a direct effect on the *Jsc* and ultimately the device efficiency. However, the UV-vis measurements do not show any systematic trend in absorption behavior and therefore trends observed in *Jsc* and device efficiency cannot be explained by the absoprtion behavior. These device properties are believed to be further complicated by the material morphology driven by a balance in wetting behavior (surface energy matching), polymer-fullerene miscibility and fullerene mobility through the polymer. To determine and understand the morphology and the role played by the interfaces in these systems experimental characterization was performed using a number of complementary techniques as discussed below.

2.3 Neutron Reflectivity

A representative set of NR data and the associated fits to the data together with the corresponding scattering length density profiles are shown in **Figure 3**. Figure 3a shows reflectivity versus momentum transfer (*Q*) plots for devices containing BHJs made of P3HT:$PC_{61}BM$ and compares the pre-annealed, post-annealed and unannealed samples. The data were fitted using RASCal software (developed at ISIS) to determine the corresponding scattering length density for the sample from which the distribution of the polymer and

fullerene in the heterojunction layer between the two electrodes is shown in Figure 3b. It is clearly evident from the NR data that the BHJ cannot be fitted as a single homogeneous layer. The simplest model that both adequately fits the data and is also consistent with all the devices measured is to consider the BHJ layer to be composed of three layers of varying thicknesses and scattering length densities. Models with more layers also fitted the data equally well, but the significance of the additional parameters these models include cannot be justified, we therefore used the simpler three-layer model in the following discussions.

With the values of the scattering length density (SLD) from the fits, the values of the volume fraction of fullerene Φ_f in the three different sub-layers were calculated using Equation 1, by assuming that the heterojunction layer is a binary mixture of polymer and fullerene and thus the component scattering length densities were additive.

$$\rho_h = \frac{\phi_p}{100}\rho_p + \frac{\phi_f}{100}\rho_f \quad (1)$$

Here ϕ_i and ρ_i are the % volume and the scattering length density of the material *i*, and the subscripts *h*, *p* and *f* refer to the heterojunction, polymer, and fullerene, respectively. The SLD values of fullerenes are significantly higher than polyalkylthiophenes, for instance for $PC_{61}BM$, $\rho_f = 4.34\times10^{-6}$ A^{-2} and for P3HT, $\rho_p = 0.74\times10^{-6}$ A^{-2}. All the calculated SLD values are tabulated in Table S2.

Using the SLD profile obtained and calculation of ϕ_f ($\phi_f + \phi_p = 100$) from Equation 1, the percentage-segregated volume of the fullerene through the depth of the BHJ was determined together with the excess volume of fullerene segregated (Equation S3 and S4) at the interfaces (given by the hatched area in Figure S5). For these calculations, mass balance of the fullerene and polymers were considered to ensure that the total composition of each is 50% when combining the results from the 3 different layers. Plots were derived for the *PCEs* values of

the same devices from the device measurements (Figure 2a) to obtain correlations and the morphological data from the NR measurement.

Three distinct layers are observed in the heterojunction for unannealed samples, a layer of fullerene enrichment near the PEDOT: PSS, a layer of fullerene depletion in the middle and a layer of fullerene depletion near the aluminum cathode as seen in the profile (green line in Figure 3 b). Upon annealing, it is seen that the fullerene enriched layers and consequently the depleted layers become further enriched and depleted respectively, compared to the pre-annealed films (red and blue lines in Figure 3b). The interface between the BHJ and Al is also seen to broaden in the devices, which is consistent with studies by other groups. [22, 25] This suggests that either the Al deposition process induces a significant degree of intermixing or more probably, Al has diffused into the bulk heterojunction layer during annealing. In order to interpret the SLD data at the electrode interfaces and convert to volume fraction of the individual BHJ components we made a number of assumptions. Firstly, we defined the region from midpoints of the BHJ interfaces with the Al on one extreme and underlying PEDOT: PSS at the other as the total BHJ film thickness. We also treated the heterojunction near the interface as only a two-component system. It is important to note was that in previously reported studies in literature [22, 25, 27, 28], the fullerene-enriched layer was considerably sharp (5 nm), compared to our samples where it is slightly more prominent (~10-15 nm), which in turn would affect the device properties substantially. Studies on a different donor-acceptor system [41] has suggested that the formation of a fullerene enrichment at the bottom electrode, depends not only on the surface energy but also on the thickness of the film and amount of polymer being spun, and thus for a thinner film with, the enrichment of the fullerene would be a considerably larger fraction of the thickness as would in our case compared to previous studies.

Given the three-layer model from the profile fitting, we thus divide the BHJ into three Zones (see **Figure 4**a). Defining the interfacial region near the aluminum surface as Zone 1, we see an enrichment of fullerene in this Zone upon post-annealing, along with an increase in roughness at the Al/BHJ interface possibly due to diffusion aluminum into the BHJ. By contrast, polymer enrichment near the Al or Ca surface is observed in the pre-annealed or unannealed devices. From the SLD values obtained in the fits, the percentage of excess fullerene in Zone 1 can be determined (Equation 1) and for the post-annealed samples this is seen to increase from around 2.3% in the case of C_{60} as the fullerene, to nearly 20 % in the case of bis-$PC_{61}BM$ in P3HT based devices(Table S6). Similar increases are seen in devices made from P3BT and P3OT as well. The thickness of Zone 1 thus remains mostly the same before and after annealing for different samples (~ 7-9 nm) but content-wise changes from a fullerene-depleted region to a fullerene enhanced region in the case of the post-annealed samples. The depletion however still remains in the case of pre annealed samples (with Ca), albeit the width of the depletion region is not as pronounced as in the case of unannealed devices. The region near the PEDOT: PSS interface is defined as Zone 3. In this Zone, an increase in SLD is observed in both the pre- and post-annealed cases, indicating fullerene enrichment in all systems. The amount of fullerene in this Zone is seen to decrease with increasing functionality as C_{60}>$PC_{61}BM$>bis-$PC_{61}BM$ (see Table S6 and S7). However, the thickness of Zone 3 varies considerably among fullerenes, as seen in Table S7. Consequently, to allow comparisons of the segregation, a normalized percentage segregated volume of the fullerene is used (equation S4, Table S6 and S7). Owing to the enrichment of fullerene at both the electrode interfaces in post-annealed samples, it is consequently depleted in the remaining bulk region, Zone 2, leading to an enrichment of the P3AT there. The three layered model proposed here is shown schematically in Figure 4a.

2.4 XPS measurements

To corroborate the NR data and subsequently correlate the segregation in the active layer in the two different device configurations i.e. with and without Ca, XPS depth profile measurements were conducted on devices that were exactly the same as for the NR measurements (see experimental). Using sulfur (S) as a critical marker of the P3AT, the depth dependency of S was used to establish the relative levels of polymer and fullerene through the BHJ film. Based on the average atomic percent content of S equal to 4.1% in a homogeneous 50:50 P3HT:$PC_{61}BM$ mixture[42], the segregation behavior of P3AT and consequently the fullerene in the BHJ layer can be determined. A representative plot of the S content as a function of etch depth through an Al/P3HT:$PC_{61}BM$/PEDOT:PSS system is shown in Figure 4b. For the pre-annealed sample, as with the results from the NR, it is clear that the P3HT is not uniformly distributed through the film thickness. The S content at the bottom interface (PEDOT PSS/BHJ) in both the cases is seen to be around 1.8% which would correspond to ~25% of P3HT at that interface and consequently 75% of $PC_{61}BM$. At the other interface (Cathode/BHJ) however, the pre-annealed case shows fullerene enrichment, corresponding to 5% S content, or ~60% P3HT or a depletion of $PC_{61}BM$ (40%). The post-annealed samples at this interface though, show an S content of around 3.2% corresponding to 40% P3HT or 60% $PC_{61}BM$ (fullerene enriched)

2.5 GIWAXS measurements

The device performance is expected to depend upon the molecular crystallography in these different Zones within the active layers, and parameters including the amount of crystallinity, crystal domain size and orientation. GIWAXS has been used to determine the in- and out-of-plane crystallography of the BHJ layer within the devices in full device configuration both before and after post-annealing (see Supplementary). Representative 2D GIWAXS patterns are shown in Figure S7-S9, where characteristic (*h00*) (h=1,2,3, etc) peaks corresponding to the polymer chain crystal planes and (*0k0*) (k=1,2,3) peaks corresponding to the polymer π-π

stacking crystal planes are labeled. The *d*-spacing for the polymer crystal stacking (d_{h00}) and π-π stacking (d_{0k0}) are calculated from the peak positions (Table S8). Using Scherrer's equation (Equation S5) and the (*100*) reflection as reference, corresponding domain sizes for the crystals were determined (Figure 7b). The crystallinity of the polymer was calculated (Table S10) while the Herman's orientation parameter, f_H, was obtained (using Equations S7 and S8) to give a value for the orientation of the *(100)* plane (see Table S9). For a comparison of the crystal orientations in the various devices and its effect on the device performance, a ratio of the edge-on to face-on contribution from the azimuthal angle integration plot was calculated (Figure S7 a). Crystals with an orientation of φ = 90° are considered to be oriented edge-on whilst those at φ = 0° have face-on crystal orientation. The areas under these respective curves and their ratios were calculated and plotted vs the J_{sc}. We observed that the edge-on composition was more prominent than the face-on (Figure 7a).

2.6 GISANS measurements

TOF-GISANS measurements were carried out to allow us to study the lateral phase structure of the BHJs at the different depths [40, 43]. Longer wavelength (lower energy) data allows us to probe the near top surface phase structure. Shorter wavelengths subsequently allowed us to probe the structure in the bulk and near bottom surface of the BHJ. The reduced 1D intensity-Q data for the highest wavelength range (6-14 Å) in all the samples measured show a distinct maxima in region $Q \sim 0.03$ Å^{-1}, which is not evident in the two lowest wavelength ranges (1.75-4 and 4-6 Å, Figure S11b). The two lowest wavelength data sets can be fitted assuming a simple Debye-Bueche two-phase structure. The highest wavelength range data was fitted using a combined model consisting of the summation of a Debye-Anderson Brumberger (DAB) model and a hard sphere model. These fits show that at all depths there are large phase-separated structures that are >200 nm in size. Given the *Q*-range of data it is not possible to give an upper range of sizes of these larger phases. In addition to the large scale

phase separation, at or near the Al/BHJ interface, the maxima in the scattering results from smaller phase-separated structures of ~4 nm. Thus, these measurements also suggest phase composition variation through the depth leading to different phase structures as observed in the GISANS profiles.

3. Discussion

3.1 Through-thickness morphology

The efficiency of a heterojunction defined by its PCEs, is calculated from the J_{sc}, V_{oc} and the FF of the devices. The short circuit current, J_{sc}, is determined from a measure of the charge generation, diffusion and collection of the light generated current[44]. It also depends on a number of external factors such as the material, optical property, exposure area as well as parameters influenced by morphology, such as charge carrier mobility and probability of charge collection, among other things. The open circuit voltage, V_{oc}, depends upon the work function of the materials used and on recombination losses[45]. Both these factors are influenced by the morphological state of the active layer. The FF in turn is related to the ratio of the maximum power output to the product of J_{sc} and V_{oc}. Therefore, any morphology that cause electronic losses through recombination or resistance would adversely affect the FF. Based on the through-thickness composition profile shown schematically in Figure 4a, we may anticipate that fullerene enrichment in Zone 1 would assist in electron transport to the aluminum electrode, thus increasing the J_{sc}. On the other hand, fullerene present in Zone 3 near the PEDOT:PSS, as seen in devices with both Al and Al/Ca electrodes, might prevent efficient charge transport to the PEDOT:PSS leading to recombination losses and consequently adversely affecting the FF. This 3 layered composition profile suggested by our NR studies was further confirmed in the XPS studies by tracking the S content through the film thickness of the BHJ, (wherein a 4.1% S content corresponded to a homogeneous 50:50 mixture of polymer and fullerene [42]). We observed a $PC_{61}BM$ %volume fraction of up to

~75% at the PEDOT:PSS interface and 40% at the Al/Ca interface on pre-annealing whereas it was up to ~60% at the post-annealed active layer/Al interface.

3.1.1 Zone 1 - As seen in Figure 3b, in our post-annealed BHJ samples, a fullerene-enriched layer is observed at the BHJ/Al interface. This is consistent with observations made previously using NEXAFS and DSIMS measurements[22] as well as neutron reflectivity for the case of P3HT/$PC_{61}BM$.[25, 46] Other studies have observed fullerene depletion at the BHJ top interface when studied without an electrode,[19] which is consistent with the behavior of the current pre-annealed devices with a BHJ/Ca interface. There is thus a clear indication of the importance of the sequence of electrode deposition and annealing which affects the segregation profile in these devices. This behavior can be rationalized by considering the surface energies of the different materials. Since the surface energy of P3HT (Γ = 26.9 mJ m^{-2}) is lower than that for $PC_{61}BM$ (Γ = 37.8 mJ m^{-2}) [47] in the absence of a capping layer, P3HT would preferentially segregate to the vacuum interface, as seen in the unannealed and pre-annealed samples. Aluminum however has a higher surface energy (Γ = 1143 mJ m^{-2})[48] than both the polymer and fullerene and thus causes the fullerene to preferentially segregate towards it when post-annealed (after electrode deposition). Similar surface energy values were theoretically calculated for the other polymer and fullerenes (Table S1) thus explaining the presence of the electron accepting fullerene near the cathode which in turn is expected to enhance the efficiency of the device.

The pre-annealed samples (Figure 3b, green line) show excess of fullerene towards the bottom and polymer excess towards the top (due to the polymers lower surface energy). As postulated by other groups previously [35, 49] the diffusion of fullerene occurs through amorphous domains of the poly(alkyl thiophene)s during annealing. Solubility between the polymer and fullerene can be estimated from interaction (binding) energies between the polymer-fullerene pairs as have been seen through our DFT measurements. According to the

initial DFT simulations conducted on the oligomer-fullerene pairs (see Figure 2b), P3BT is expected to have the greatest miscibility with the fullerenes, presumably due to the short alkyl-chains not sterically hindering backbone interactions with the fullerene. Larger amount of fullerene miscibility for shorter side-chain polymer causes greater movement through the polymer amorphous region (and segregation) towards the top of the active layer (P3BT>P3HT>P3OT). In contrast, larger side chains (P3OT>P3HT>P3BT) lead to lower polymer crystallinity (Figure S10), allowing easier diffusion of fullerenes on annealing and lead to phase segregation of the polymer-fullerene through the bulk of the material in an opposing trend[50]. This combined with the interfacial effect of surface energy from the electrode, which drives the fullerene to move towards the surface, explains the greater segregation of the fullerenes to Zone 1 on post-annealing. A mix of these three counteracting, thermodynamic (miscibility, surface energy) and kinetic (diffusion) factors thus ensures that the optimal phase separation of fullerene occurs in the P3HT:electron acceptor active layer near the cathode (Figure 3b, red line) which in turn facilitates electron transport and improves the efficiency.

Plots of both the J_{sc} and segregated volume of fullerene in Zone 1 versus the number of carbon atoms in the P3AT alkyl chain are shown in **Figure 5** *a* and b. We see that the amount of segregation for all the three fullerenes is a maximum in devices with P3HT (Figure 5a). At the same time, the highest J_{sc} observed when comparing the polymer is also with P3HT for any of the fullerenes. This behavior can be better understood when directly comparing fullerene segregation in Zone 1 against the J_{sc} in these devices as shown in Figure 5c. In this plot it is clear that there is a linear dependence between segregated amounts of fullerene at the Al/BHJ interface and the device $J_{sc.}$

3.1.2 Zone 3 – In Zone 3 fullerene segregation is observed near the PEDOT:PSS interface (Figure 3b, red and blue line) in all the devices, with or without Ca. The segregated fullerene

volume is somewhat more prominent in pre-annealed devices than in post-annealed (Figure 3b). Compared to the unannealed samples, a considerable amount of fullerene, after annealing (both pre and post) is seen to shift towards the Al electrode, but the concentration of fullerene is still considerably enhanced near the PEDOT: PSS interface.

For post annealed devices (with Al electrode) the fullerene rich content and layer thickness in Zone 3 is greatest in BHJ devices with P3BT (see Table S6 and 5), which also seems to be inverse to the behavior seen in device performances (as seen Figure 2a, P3BT devices having the lowest efficiency). This again implies, as discussed for Zone 1, that the length of side chain affects the degree of fullerene segregation, and the amount of fullerene segregated towards the PEDOT:PSS interface may be used to predict changes in device performance. Before annealing, the devices have segregated fullerene in Zone 3 (Figure 3b, green line), which has been attributed to the fact that fullerenes are more soluble in the o-DCB than in the polymers.[51] Consequently, during evaporation of the solvent during spin coating, due to the nature of solvent drying, the fullerene stays in the solution near the bottom of the substrate till it dries up.[52] (See Table S2 for Hansen solubility parameters)[53] Upon annealing, the fullerene diffuses to the Al/BHJ interface, much more easily in the case of P3OT than with the other polymers. This diffusion is also much more pronounced for the case of post-annealing where fullerene movement is also driven by Al/BHJ interfacial surface energy effects, than just thermal effects (of annealing) in case of pre-annealed samples where the top interface is absent during annealing. Despite the movement of the fullerene, a thin layer of fullerene still remains on this interface after annealing, due to the matching of the PEDOT PSS surface energy (72.88 mJ/m^2) [54] to the higher surface energy of the fullerene, as compared to the polymer. When the *FF* and the segregated fullerene in Zone 3 (Tables S6 and S7) are compared to each other, a correlation between these parameters is observed in both device types, i.e., with and without Ca (see **Figure 6**). This correlation of a reduction in FF with

increasing fullerene segregation at the PEDOT:PSS interface is consequently stronger for the post-annealed devices/without Ca (Figure 6a). The behavior strongly indicates that excess fullerene in the vicinity of the PEDOT:PSS hole transport layer inhibits hole transport.

Even though the excess fullerene content at this interface for P3HT and P3OT showed marginal differences (~ 6.5 and 6.9 % respectively for the $PC_{61}BM$ based devices, Table S7) the *FF* is highest for the P3HT: fullerene systems (compared to the other two polymers). This suggests that other factors such as the morphological structure of the fullerene-polymer system at the interface might also be of importance. Hole transport that occurs through the polymer, would be affected by the nature of the morphology in and around the polymer, both locally i.e., crystallinity, and macroscopically, i.e., phase behavior. Excess fullerene segregtion at the PEDOT:PSS interface adversely affects continuity of polymer phases and thereby hole transport would consequently be inhibited, leading to a reduction in the fill factor.

In addition, studies on the interfacial effects on device performance have to take into consideration the interfacial roughness. In P3BT-C_{60} heterojunctions, in addition to fullerene segregation, we also see that the roughness of the P3BT-C_{60} at the PEDOT:PSS interface is extremely high[55] at both the interfaces, and a smooth enough heterojunction film of the same is difficult to obtain. Heterojunction film roughness for all the devices obtained from NR measurements are thus seen to adversely affect the FF considerably and lead to lower device performance (Table S6 and S7). The film roughness can be attributed to the low miscibility (leading to phase segregation) of C_{60} in P3BT and the solvent (discussed later through GIWAXS measurements (Figure S9 b)). Miscibility thus plays an important role in the film formation and its roughness, consequently affecting the fill factor and device performance

3.1.3 Annealing effects – It has been determined that for very thin BHJ films, as in the current work (~80 nm), the J_{sc} is very low compared to P3HT:$PC_{61}BM$ systems that have optimized in thicker films.[56] It was seen that device efficiency improved after post-annealing in the

absence of Ca, whereas post-annealing had a detrimental effect on the efficiency in the presence of a Ca layer. The effect of the presence of Ca at the Al cathode interface after post-annealing has been observed previously, and was explained by the small Ca atoms diffusing into the active layer [57] or Ca oxidation [36], during annealing, causing a reduction in the efficiency of the device.

On annealing, recrystallization of the polymer occurs whilst simultaneously causing phase segregation within the active layer.[11] The enhanced polymer crystallinity leads to increased hole mobility and hence increased J_{sc}.[5, 58] In addition, when the samples are post-annealed with the electrode in place, the increased segregation of fullerene towards the Al interface due to surface energy differences, as discussed earlier, also enhances the J_{sc}. In our case, because the BHJ films are slightly thinner than the convention, the device properties are even more likely to be dominated by the interfacial effects, where the relative proportion of segregated volume fraction compared to the overall BHJ layer thickness will be large. This is therefore more likely a bigger cause of increase in J_{sc} compared to thicker films.

3.2 Lateral Morphology

The GIWAXS results show changes in the crystal orientation (**Figure 7**a), crystal domain size (Figure 7b), and an increase in the crystallinity in the different systems upon annealing (Figure S7-S9, Table S6-S8). Increasing crystalline domain size and orientation of the crystals, upon annealing, both have an influence on J_{sc}. The closer the domain size approaches the exciton diffusion length (typically ~8-10 nm in these materials [13]), the higher is the probability that formed excitons diffuse to an interface and dissociate rather than recombine. In this domain size range the system is expected to produce the maximum charge generation as is seen in our devices too (Figure 7b). At the same time, orientation of the crystals with a face-on orientation relative to the substrate would be conducive to charge transport and thus a larger face-on contribution of crystals correlates to a better charge generation and hence an

increase in J_{sc}. Thus we see that the P3HT, (Figure 7a) which shows the smallest edge-on to face-on ratio (consequently maximum amount of face on orientation) in these devices, results in the highest J_{sc}. This correlation is more strongly valid for the case where there is limited large-scale phase separation occurring in the active layer. Phase separation usually isn't prevalent in pre-annealed samples, but it might develop in post-annealed samples due to the high boiling point solvent used (o-dichlorobenzene), which would evaporate slowly and over time promote fullerene aggregation. This is especially true in the case of devices made with C_{60} fullerene (Figure S9 a and b), where the active layer has large fullerene aggregates (~10 nm) in the bulk that are phase segregated due to poor miscibility with the polymers. Due to the reduced miscibility (based on the binding energy calculation values, Figure 2b), C_{60} devices would consequently also have the least amount of molecularly dispersed fullerene in the amorphous polymer regions, which reduce efficient charge separation in the device (exciton separation occurring at the polymer-fullerene interfaces). Limited miscibility of fullerenes also causes device roughness at the interface and these effects, combined, would adversely affect the J_{sc} and PCE as we see in C_{60} based devices in Figure 2a.

Taking the lateral (in-plane) morphology, crystal structure and orientation into consideration, the possible overall morphological structure in the active layer for post-annealed BHJ devices can be hypothesized as shown in **Figure 8**. From the NR measurements, we obtain a through-thickness profile of fullerene segregation at the interfaces and the GIWAXS measurement suggests multiple phases in the system including regions of crystalline polymers, fullerene dispersed in amorphous polymer phases and phase segregated excess fullerene. The lateral morphology can be understood from the GISANS measurements at three different wavelength ranges (Figure S11a) corresponding to three different depth scales corresponding, i.e., Al/active layer interface (Zone 1), intermediary bulk Zone (Zone 2) and the active layer/PEDOT: PSS interface (Zone 3). From the fitting of the three plots, firstly characteristic

domain sizes of ~6 nm were seen in Zone 1 together with larger domains that are >200 nm (Figure S11b, blue line). The smaller domains are considered to be in the right size range to be ideal for exciton diffusion and dissociation, in addition to providing the channels transporting the electronic charges the Al electrode. The SLD values for the fit (Table S11) suggest the smaller domains to be in the shape of hard sphere based on pure fullerene and the larger domains consisting of a mixture of fullerene and polymer. This explains the excess fullerene content and its strong correlation to the J_{sc} in this region. In Zone 2 (Figure S11b, red line), the small domains (pure fullerene) are absent and only the single larger phase (mixture of amorphous polymer-fullerene) structures are found, suggesting the absence of fullerene enrichment and phase segregation in this region. Given the average compositions through the film thickness determined from the NR, these domains are thought to be polymer-rich phases. Similarly in Zone 3 (Figure S11b, black line) although the *Q*-range is limited, there is no suggestion of smaller domains in this region and only scattering consistent with large-scale (>200 nm) domain structures is observed. In this region, though these large-scale domains must be assumed to be fullerene-rich and since these phases have a higher SLD values (commensurate with larger amount of fullerene molecules) as to the comparative ones in Zone 2 (Table S11).

Thus for the overall morphological structure (Figure 8), we theorize that the active layer contains mainly a dispersion of segregated fullerene in polymer or domains of pure polymer crystals and fullerene with some regions of fullerene molecularly dispersed in amorphous polymer.[39] Taking into consideration the depth-dependent GISANS experiments Zone 1 would have distinct fullerene domains (hard spheres) due to it being in excess, and some small amount of fullerene dispersed in the amorphous phases of the polymer. It would also contain a large phase of polymer-fullerene amorphous mixture along with polymer crystallites. The bulk (Zone 2), having a more homogenous composition (with slight polymer excess)

would thus have only the polymer crystallites and similar polymer-fullerene amorphous mixtures characterized by large domain sizes. For the last Zone (Zone 3), even though GISANS analysis isn't definitive, the available data allows us to predict that we would see similar large domains of amorphous polymer fullerene mixture, with slightly greater amount of fullerene than in the bulk.

3.3 BHJ with spin-coated Fullerene Adlayer

To test the hypothesis that fullerene enrichment has a significant effect on device behavior and specifically the J_{sc}, P3HT:$PC_{61}BM$ devices with and without Ca were prepared with an additional $PC_{61}BM$ layer deliberately deposited between the BHJ and the Ca/Al interface. The additional layer was placed so that it would serve as an electron transport layer at the BHJ-cathode interface, thereby enhancing the charge collection and consequently the J_{sc}. The presence of a pure $PC_{61}BM$ layer on the top was confirmed by an XPS measurement, by detecting the absence of sulfur at the top layer (Figure S12). For both device types, a distinct improvement in J_{sc} was observed (see **Table 1**), with a 20% improvement seen for Ca/Al containing devices compared to 8% improvement for devices without Ca. These differences in improvement are possibly because the pre-annealed devices (without an adlayer) did not start off with a fullerene-enriched layer and so the addition of an extra fullerene layer acted as an electron transport layer for the device. By comparison the post-annealed devices already had a segregated fullerene layer as the cathode, which leads to an enhancement of its J_{sc}. These results completely support our hypothesis that the fullerene segregation to the device cathode directly affects the short circuit current and consequently provides valuable design strategies for improving device performance.

4. Conclusions

Neutron reflectivity and XPS measurements show that the bulk heterojunction in OPVs is not homogeneous throughout its thickness but can be considered to be stratified into three Zones,

with fullerenes predominantly segregated at the two electrode interfaces leaving the central layer of the film polymer-rich. The segregation of the fullerene in the different P3AT-fullerene devices was correlated with the device performance values through either the J_{sc} or *FF* parameters. The degree of interfacial segregation of the fullerenes is a balance in wetting behavior (surface energy matching), polymer-fullerene miscibility and fullerene mobility through the polymer. Differences in polymer-fullerene solubility ensure lower interfacial roughness of films at the top electrode initially, while thermal annealing (post electrode depositing) leads to greater segregation of fullerenes towards the cathode (and away from the anode). Greater fullerene segregation at the cathode promotes better electron transport and thus improves the J_{sc} and consequently the device performance. The fullerene at the anodic interface has the opposing effect in terms of promoting charge recombination, thus reducing the fill factor and consequently, hinders efficient device performance. Based on this knowledge, we have demonstrated the significance of fullerene segregation to the cathode by deliberately building devices with a spin-coated fullerene adlayer at the cathode, which increased the device performance with an improvement in the J_{sc} of 20%.

The morphology of the BHJ is complex and shows that the lateral structure is also depth dependent. Using GISANS and GIWAXS we have shown the importance of having controlled depth dependent phase morphology along with face-on polymer crystal orientation, and domain size (~10nm), for an optimally performing device. However it can be inferred that the effect on the PCE of a device depends on the combined evolution of a number of varied morphological factors, some of which, such as the polymer segregation, interfacial depletion, have been discussed here.

5. Experimental

5.1 Solvent ratio and concentration

The bulk heterojunction samples were prepared using P3AT (poly-3alkylthiophenes) and a choice of three different fullerene derivatives, C_{60} (fullerene), $PC_{61}BM$, bis-$PC_{61}BM$. Different combinations of polymer and fullerene were tried to give us nine different heterojunctions.

The solvent chosen was ortho-dichlorobenzene (o-DCB) since it has seen to give better solubility, crystal packing and uniformity in the film thickness in comparison to other solvents such as toluene, and chloroform. Ref 1. Solutions of 0.8% (wt/vol) of all the compounds in O-DCB were prepared and then mixed in 1:1 (polymer: fullerene) ratio.

5.2 Device Fabrication

The bulk heterojunction type solar cells for NR, GISANS and GIWAXS measurements were prepared on silica substrates of 1" by 1". A layer of SiO_2 of ~300 nm thickness was deposited on top of the substrate using PECVD. PEDOT: PSS diluted solution (1:6 with water) was used to obtain very thin layers ~ 10nm by spin coating on the oxide layer using water as the solvent using a spin speed of 1200 rpm for 10 sec, followed by 4000 rpm for 60 sec. The layer was subsequently was dried by heating at 150 C for 10 mins. The BHJ mixtures were then spin coated from the previously prepared solutions directly onto the PEDOT: PSS layer at a speed of 1500 rpm for 40 seconds to give layers in the thickness of ~ 40 nm. The BHJ were finally capped on top by the aluminum (~60nm) cathode layer by thermal evaporation onto the film surface, covering the entire active layer area.

Solar cell devices were fabricated on ITO-glass substrates with a square resistance 10 $\Omega \cdot cm^2$. The substrates were initially washed using detergent and rinsed in pure water, followed by ultra-sonication sequentially in acetone and isopropanol. The substrates were dried in oven overnight prior to use. ITO-glass substrates were UV-plasma treated and a ~40nm thick PEDOT: PSS layer was deposited on the substrates. Then BHJ composites were spun cast directly on top of PEDOT: PSS layer in a N_2 filled glove box from pre-prepared solution.

Finally, 100 nm of aluminum was thermally evaporated onto the BHJ layers under high vacuum of a minimum of 4×10^{-4} Pa.

Pre-annealed BHJs were annealed at 120 °C for 20 minutes before electrode deposition (Ca/Al) and while post-annealed devices were annealed at 150 °C for 20 min after electrode deposition (Al) under N_2 gas.

Solar cell devices with $PC_{61}BM$ electron transport layer were made similar to regular ones with the additional step of an extra layer of $PC_{61}BM$ solution (5 mg/mL) spun from a orthogonal solvent (DCM) at 1500 RPM for 30 seconds to give us layers of thickness ~5-10 nm

5.3 Neutron Reflectivity

Neutron reflectivity (NR) was performed on the devices of P3AT:fullerene prepared on (2.5×2.5)cm samples using the CRISP and SURF instruments at the ISIS Facility, Rutherford Labs, Oxford, UK. The wavelength range was 0.5-6.5A. Reflectivity data were collected over 2 or 3 angles with constant dQ/Q resolution giving a combined *Q*-range from 0.008 - ~0.2 $Å^{-1}$. In comparison to the devices, the samples used here had the electrodes (Al or Al/Ca) completely covering the active layer. The raw data was reduced to obtain Intensity vs Q data using the software MANTID and analyzed for fitting using the software RAScal. The fitting program was carried out utilizing alternatively a combination of the Nelder-Mead Simplex Method and the Marquardt-Levenberg method.

5.4 XPS measurement

Were performed in the shared user laboratory of the Georgia Tech IEN Organic Cleanroom. The machine used was a Thermo K-alpha XPS, with an X-ray source. Depth profiles were obtained by repeated standard XPS measurements followed by sample etching using an Argon ion source. Etching was achieved using an ion source energy of 3000 eV with etch periods of

100s between each measurement. Each etch cycle was found to correspond to the etching of BHJ film thickness of ~8 nm. Due to differences in etching rates, for the same ion source energy, 100s of etching of Al resulted in film thickness changes of only 2 nm.

5.5 GIWAXS measurement

Were carried out on beamline 11-3 at the Stanford synchrotron radiation light source (SSRL). The beam was kept at an energy of 13 KeV and the critical angle of measurement was 0.12 **°.** A LaB_6 standard sample was used to calibrate the measurements. The 2-D images were reduced to 1-D plots and analyzed using the software WxDiff. Peak fitting was done using the software MagicPlot Pro. In-situ annealing measurement was carried out in a using a thermocouple in the sample chamber under inert conditions (He gas). Annealing temperature and time were the same as that used for the post annealed devices mentioned earlier.

5.6 GISANS measurement

Were carried out on the SANS2D instrument at the ISIS Facility. The measurements were made using a wavelength range of 1.75 – 14 Å. With measurements made at fixed incident angle (θ = 0.35°), the critical edge of the samples occurs at 6 Å. Consequently indirect depth sensitivity is achieved by evaluating the scattering behavior as a function of wavelength above and below this critical wavelength. The measurement were over three wavelength ranges (1.75-4 Å, 4-6 Å and 6-14 Å) corresponding to the three energy levels of the neutron beam, giving us scattering through the thin film at different depths.

5.7 **UV-vis absorption measurements**

Thin films for UV-vis absorption measurements were spin coated on to pre-cleaned glass substrates from 5 mg/ml (total) o-dichlorobenzene solutions of the different P3AT:fullerene mixtures at the spin speeds of 1200 rpm. Absorption measurements were carried out using a Varian Cary 5E UV-vis-NIR spectrophotometer over the wavelength range of 300-800 nm.

The thicknesses of the films were measured using a Bruker DektakXT profilometer and used to normalize the absorption measurements.

5.8 DFT calculations

All-electron DFT calculations within the local density (LDA) and generalized gradient approximations (GGA) as implemented in NWChem[59] was used to determine geometries for fullerene and its derivatives interacting with oligomers of the polyalkylthiophene structures shown in Figure S1. The initial geometries for the different polymer-fullerene systems were obtained by optimizing the geometry via energy minimization of the fullerene-alkylthiophene oligomers using Materials Studio 5.0 (Accelrys). The Fletcher Reeves algorithm and the Newton (BFGS algorithm) methods were used to achieve the initial minimization. Subsequently, a NVT molecular dynamics simulation was run on the lowest energy structures using a Nose-Hoover thermostat at 298 K. These local energy minimum structures were run through the energy minimization protocol again to obtain the initial input structures for the DFT calculations.

For DFT calculations, the DFT-D method[60] was used to obtain the non-bonded interactions between the fullerene-polymer pairs. The gas phase fullerene-alkylthiophene monomer interaction energies were computed by

$$E_B B = E_{mf} - E_{BSSE} - E_{def} \quad (2)$$

where E_b is the binding energy[61]. E_{mf} is the energy of the optimized polymer-fullerene pair and E_{BSSE} is a calculation of the basis set superposition error (BSSE) defined by $E_{BSSE} = \sum i\ E_i$ (g), where E_i (g) is the energy of the alkylthiophene monomer or fullerene at the geometry in the pair (fullerene-alkylthiophene) with pair basis functions present. E_{def} was the deformation energy, calculated by the equation $E_{def} = \sum i\ [E_i\ (opt) - E_i]$, where E_i (opt) is the energy of the optimized species (fullerene or oligomer).

Acknowledgements

We gratefully acknowledge partial support from by the U.S. Department of Energy, Division of Basic Energy Sciences under contract No. DE-FG02-10ER4779. We also thank ISIS Facility, Harwell, UK for neutron beam time access for the GISANS measurements on SANS2D, and SSRL, Stanford, USA for GIWAXS beam time access on beam line 11-3. We also thank Dr S. Rogers and Dr C. Tassone for help during these measurements. The work by BGS was performed at the Center for Nanophase Materials Sciences, a DOE Office of Science User Facility.

References

[1] Lewis, N. S. ; Crabtree, G. ; Nozik, A. J. ; Wasielewski, M. R. ; Alivisatos, P. ; Kung, H. ; Tsao, J. ; Chandler, E. ; Walukiewicz, W. ; Spitler, M. ; Ellingson, R. ; Overend, R. ; Mazer, J. ; Gress, M. ; Horwitz, J. ; Ashton, C. ; Herndon, B. ; Shapard, L. ; Nault, R. M.; Basic Research Needs for Solar Energy Utilization, Report of the Basic Energy Sciences Workshop on Solar Energy Utilization, April 18-21, 2005, Office of Science, U.S. Department of Energy, 2005 (http://www.osti.gov/scitech/biblio/899136; last accessed 2 Dec 2015)

[2] Solar Energy Perspectives, International Energy Agency, 2011 (http://www.iea.org/publications/freepublications/publication/solar-energy-perspectives.html last accessed 2 Dec 2015).

[3] C. Liu, C. Yi, K. Wang, Y. Yang, R. S. Bhatta, M. Tsige, S. Xiao, X. Gong, ACS Applied Materials & Interfaces 2015, 7, 4928.

[4] J. You, L. Dou, K. Yoshimura, T. Kato, K. Ohya, T. Moriarty, K. Emery, C.-C. Chen, J. Gao, G. Li, Y. Yang, Nat Commun 2013, 4, 1446.

[5] W. Ma, C. Yang, X. Gong, K. Lee, A. J. Heeger, Advanced Functional Materials 2005, 15, 1617.

[6] *NREL efficiency chart*, NREL, 2014.

[7] C. J. Brabec, S. Gowrisanker, J. J. M. Halls, D. Laird, S. Jia, S. P. Williams, Advanced Materials 2010, 22, 3839.

[8] H. Hoppe, N. S. Sariciftci, Journal of Materials Chemistry 2006, 16, 45.

[9] M. T. Dang, L. Hirsch, G. Wantz, Advanced Materials 2011, 23, 3597; T. M. Clarke, J. R. Durrant, Chem Rev 2010, 110, 6736; Y. Kim, S. Cook, S. M. Tuladhar, S. A. Choulis, J. Nelson, J. R. Durrant, D. D. C. Bradley, M. Giles, I. McCulloch, C.-S. Ha, M. Ree, Nat Mater 2006, 5, 197; S. Günes, H. Neugebauer, N. S. Sariciftci, Chemical Reviews 2007, 107, 1324.

[10] G. Dennler, M. C. Scharber, C. J. Brabec, Advanced Materials 2009, 21, 1323.

[11] S. van Bavel, E. Sourty, G. de With, K. Frolic, J. Loos, Macromolecules 2009, 42, 7396.

[12] G. Yu, J. Gao, J. C. Hummelen, F. Wudl, A. J. Heeger, Science 1995, 270, 1789.

[13] P. E. Shaw, A. Ruseckas, I. D. W. Samuel, Advanced Materials 2008, 20, 3516.

[14] J. Zhao, A. Swinnen, G. Van Assche, J. Manca, D. Vanderzande, B. V. Mele, The Journal of Physical Chemistry B 2009, 113, 1587; F. Liu, Y. Gu, J. W. Jung, W. H. Jo, T. P. Russell, Journal of Polymer Science Part B: Polymer Physics 2012, 50, 1018.

[15] D. Chirvase, J. Parisi, J. C. Hummelen, V. Dyakonov, Nanotechnology 2004, 15, 1317.
[16] N. D. Treat, M. A. Brady, G. Smith, M. F. Toney, E. J. Kramer, C. J. Hawker, M. L. Chabinyc, Advanced Energy Materials 2011, 1, 82.
[17] H. Chen, J. Peet, Y.-C. Hsiao, B. Hu, M. Dadmun, Chemistry of Materials 2014, 26, 3993; N. Deb, R. R. Dasari, K. Moudgil, J. L. Hernandez, S. R. Marder, Y. Sun, A. Karim, D. G. Bucknall, Journal of Materials Chemistry A 2015, 3, 21856.
[18] D. Chen, F. Liu, C. Wang, A. Nakahara, T. P. Russell, Nano Letters 2011, 11, 2071.
[19] W.-R. Wu, U. S. Jeng, C.-J. Su, K.-H. Wei, M.-S. Su, M.-Y. Chiu, C.-Y. Chen, W.-B. Su, C.-H. Su, A.-C. Su, ACS Nano 2011, 5, 6233.
[20] X. Yang, J. Loos, S. C. Veenstra, W. J. H. Verhees, M. M. Wienk, J. M. Kroon, M. A. J. Michels, R. A. J. Janssen, Nano Letters 2005, 5, 579.
[21] D. S. Germack, C. K. Chan, B. H. Hamadani, L. J. Richter, D. A. Fischer, D. J. Gundlach, D. M. DeLongchamp, Applied Physics Letters 2009, 94, 233303.
[22] D. Chen, A. Nakahara, D. Wei, D. Nordlund, T. P. Russell, Nano Letters 2010, 11, 561.
[23] S. S. van Bavel, M. Bärenklau, G. de With, H. Hoppe, J. Loos, Advanced Functional Materials 2010, 20, 1458.
[24] A. J. Parnell, A. D. F. Dunbar, A. J. Pearson, P. A. Staniec, A. J. C. Dennison, H. Hamamatsu, M. W. A. Skoda, D. G. Lidzey, R. A. L. Jones, Advanced Materials 2010, 22, 2444; J. W. Kiel, B. J. Kirby, C. F. Majkrzak, B. B. Maranville, M. E. Mackay, Soft Matter 2010, 6, 641.
[25] C. W. Rochester, S. A. Mauger, A. J. Moulé, The Journal of Physical Chemistry C 2012, 116, 7287.
[26] S. A. Mauger, L. Chang, S. Friedrich, C. W. Rochester, D. M. Huang, P. Wang, A. J. Moulé, Advanced Functional Materials 2013, 23, 1935.
[27] H. Lu, B. Akgun, T. P. Russell, Advanced Energy Materials 2011, 1, 870.
[28] H. Kim, W.-W. So, S.-J. Moon, Solar Energy Materials and Solar Cells 2007, 91, 581.
[29] C. H. Woo, B. C. Thompson, B. J. Kim, M. F. Toney, J. M. J. Fréchet, Journal of the American Chemical Society 2008, 130, 16324.
[30] M. A. Ruderer, S. Guo, R. Meier, H.-Y. Chiang, V. Körstgens, J. Wiedersich, J. Perlich, S. V. Roth, P. Müller-Buschbaum, Advanced Functional Materials 2011, 21, 3382.
[31] W.-H. Baek, H. Yang, T.-S. Yoon, C. J. Kang, H. H. Lee, Y.-S. Kim, Solar Energy Materials and Solar Cells 2009, 93, 1263.
[32] E. Verploegen, R. Mondal, C. J. Bettinger, S. Sok, M. F. Toney, Z. Bao, Advanced Functional Materials 2010, 20, 3519; N. D. Treat, C. G. Shuttle, M. F. Toney, C. J. Hawker, M. L. Chabinyc, Journal of Materials Chemistry 2011, 21, 15224.
[33] E. Verploegen, C. E. Miller, K. Schmidt, Z. Bao, M. F. Toney, Chemistry of Materials 2012, 24, 3923.
[34] J. W. Kiel, A. P. R. Eberle, M. E. Mackay, Physical Review Letters 2010, 105, 168701.
[35] W. Yin, M. Dadmun, ACS Nano 2011, 5, 4756.
[36] B. Paci, A. Generosi, V. Rossi Albertini, P. Perfetti, R. de Bettignies, C. Sentein, Chemical Physics Letters 2008, 461, 77.
[37] M. Jørgensen, K. Norrman, F. C. Krebs, Solar Energy Materials and Solar Cells 2008, 92, 686.
[38] M. Lenes, G.-J. A. H. Wetzelaer, F. B. Kooistra, S. C. Veenstra, J. C. Hummelen, P. W. M. Blom, Advanced Materials 2008, 20, 2116.
[39] M. A. Ruderer, R. Meier, L. Porcar, R. Cubitt, P. Müller-Buschbaum, The Journal of Physical Chemistry Letters 2012, 3, 683.
[40] P. Müller-Buschbaum, E. Maurer, E. Bauer, R. Cubitt, Langmuir 2006, 22, 9295.

[41] R. Meier, M. A. Ruderer, A. Diethert, G. Kaune, V. Körstgens, S. V. Roth, P. Müller-Buschbaum, The Journal of Physical Chemistry B 2011, 115, 2899.
[42] V. Brand, C. Bruner, R. H. Dauskardt, Solar Energy Materials and Solar Cells 2012, 99, 182.
[43] P. Müller-Buschbaum, L. Schulz, E. Metwalli, J. F. Moulin, R. Cubitt, Langmuir 2008, 24, 7639.
[44] J.-L. Brédas, J. E. Norton, J. Cornil, V. Coropceanu, Accounts of Chemical Research 2009, 42, 1691.
[45] M. C. Scharber, D. Mühlbacher, M. Koppe, P. Denk, C. Waldauf, A. J. Heeger, C. J. Brabec, Advanced Materials 2006, 18, 789.
[46] Z. Sun, K. Xiao, J. K. Keum, X. Yu, K. Hong, J. Browning, I. N. Ivanov, J. Chen, J. Alonzo, D. Li, B. G. Sumpter, E. A. Payzant, C. M. Rouleau, D. B. Geohegan, Advanced Materials 2011, 23, 5529.
[47] J. W. Jung, J. W. Jo, W. H. Jo, Advanced Materials 2011, 23, 1782.
[48] L. Vitos, A. V. Ruban, H. L. Skriver, J. Kollár, Surface Science 1998, 411, 186.
[49] M. Campoy-Quiles, T. Ferenczi, T. Agostinelli, P. G. Etchegoin, Y. Kim, T. D. Anthopoulos, P. N. Stavrinou, D. D. C. Bradley, J. Nelson, Nat Mater 2008, 7, 158.
[50] L. H. Nguyen, H. Hoppe, T. Erb, S. Günes, G. Gobsch, N. S. Sariciftci, Advanced Functional Materials 2007, 17, 1071.
[51] P. A. Troshin, H. Hoppe, J. Renz, M. Egginger, J. Y. Mayorova, A. E. Goryochev, A. S. Peregudov, R. N. Lyubovskaya, G. Gobsch, N. S. Sariciftci, V. F. Razumov, Advanced Functional Materials 2009, 19, 779.
[52] B. Tremolet de Villers, C. J. Tassone, S. H. Tolbert, B. J. Schwartz, The Journal of Physical Chemistry C 2009, 113, 18978.
[53] D. W. V. Krevelen, K. T. Nijenhuis, *Properties of Polymers: Their Correlation with Chemical Structure; their Numerical Estimation and Prediction from Additive Group Contributions*, Elsevier Science, 2009.
[54] M. Petrosino, A. Rubino, Synthetic Metals 2012, 161, 2714.
[55] T. Wang, A. J. Pearson, D. G. Lidzey, R. A. L. Jones, Advanced Functional Materials 2011, 21, 1383.
[56] A. J. Moule, J. B. Bonekamp, K. Meerholz, Journal of Applied Physics 2006, 100, 094503.
[57] H. Jin, M. Tuomikoski, J. Hiltunen, P. Kopola, A. Maaninen, F. Pino, The Journal of Physical Chemistry C 2009, 113, 16807.
[58] G. Li, V. Shrotriya, J. Huang, Y. Yao, T. Moriarty, K. Emery, Y. Yang, Nat Mater 2005, 4, 864.
[59] R. A. Kendall, E. Aprà, D. E. Bernholdt, E. J. Bylaska, M. Dupuis, G. I. Fann, R. J. Harrison, J. Ju, J. A. Nichols, J. Nieplocha, T. P. Straatsma, T. L. Windus, A. T. Wong, Computer Physics Communications 2000, 128, 260.
[60] L. A. Burns, Á. V.-. Mayagoitia, B. G. Sumpter, C. D. Sherrill, The Journal of Chemical Physics 2011, 134, 084107.
[61] D. Linton, P. Driva, B. Sumpter, I. Ivanov, D. Geohegan, C. Feigerle, M. D. Dadmun, Soft Matter 2010, 6, 2801; K. Campbell, B. Gurun, B. G. Sumpter, Y. S. Thio, D. G. Bucknall, J Phys Chem B 2011, 115, 8989.

Figures and Tables

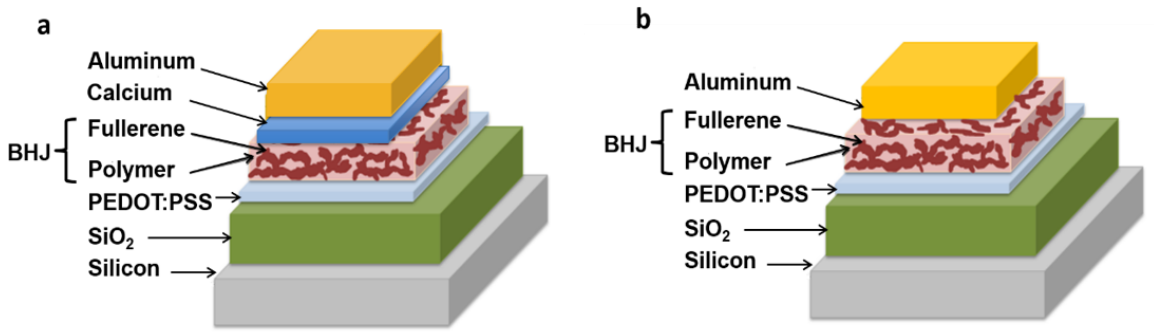

Figure 1. Layers in the bulk heterojunction device structure (for device characterization and performance measurements) of polymer-fullerene mixtures (polyalkylthiophenes with modified fullerenes) a) with Ca b) without Ca (Si/SiO_2 replaced by ITO/Glass for performance measurements)

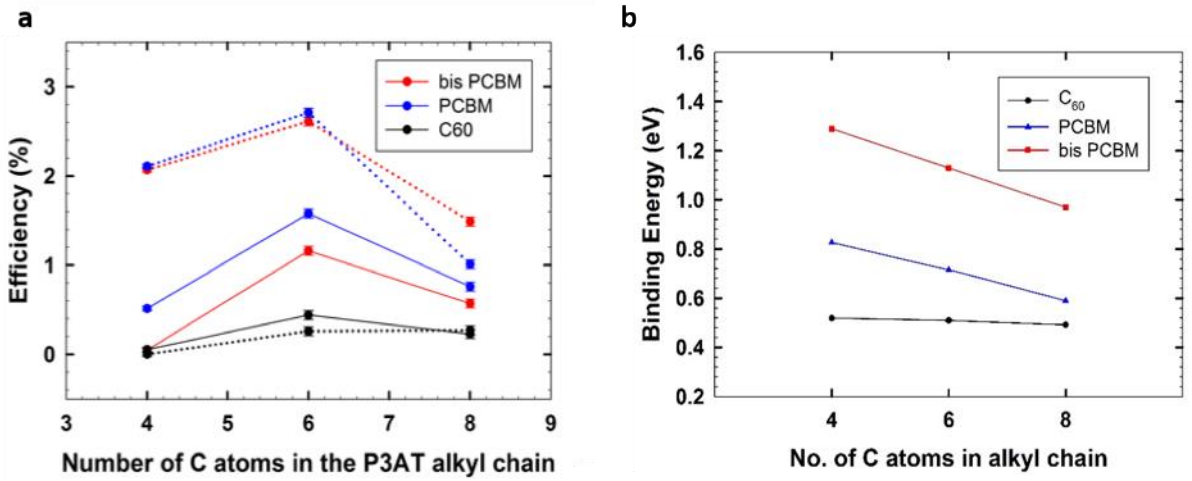

Figure 2.a) Power conversion efficiency values, for the different P3AT-fullerene systems in device form with Ca (dashed) and without Ca (solid line) b) Binding Energy vs alkyl chain length of the polyalkylthiphene for the different mixtures

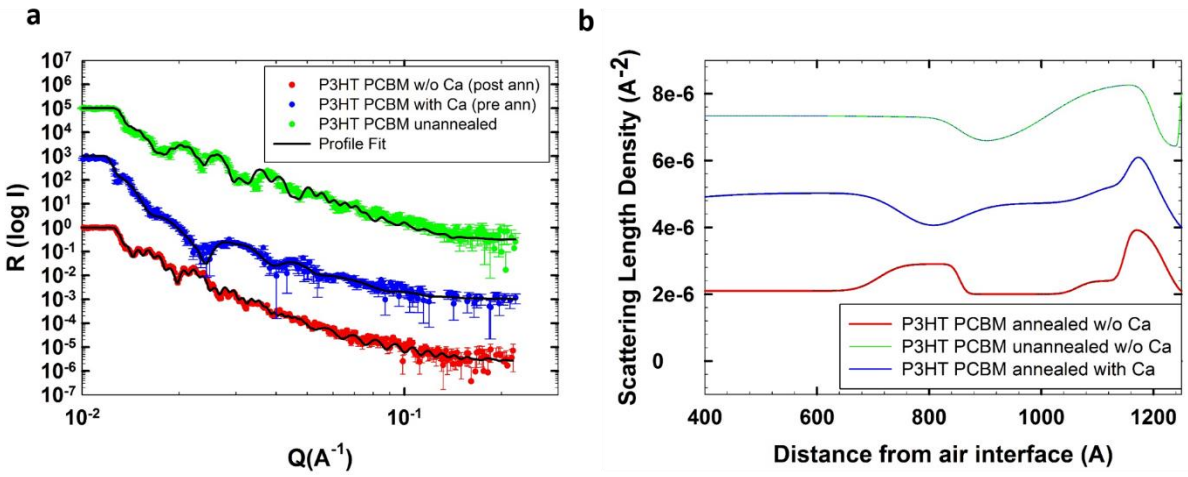

Figure 3 a) Neutron reflectivity plots (Reflectivity vs momentum transfer) for pre- and post-annealed P3AT: $PC_{61}BM$ devices b) SLD profile through the layers in the heterojunction device, for pre- and post-annealed P3HT:$PC_{61}BM$ systems. (Profile starting at 400 Å to show zoom-in of the BHJ active layer starting ~ 600 Å)

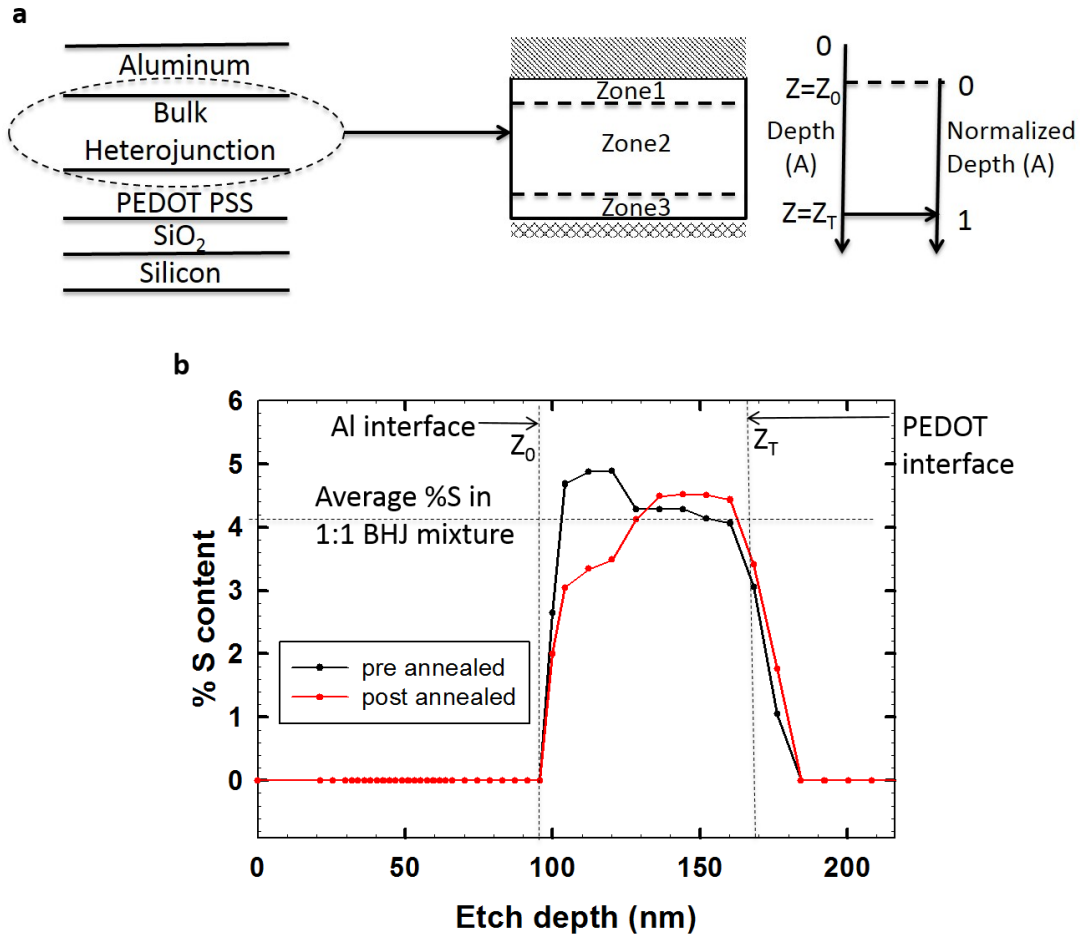

Figure 4. a) Proposed general structure of the heterojunction that is composed of 3 layers as determined from NR b) Atomic percent of S as a function of XPS depth profiling through P3HT:$PC_{61}BM$ based device structure, pre- and post-annealed

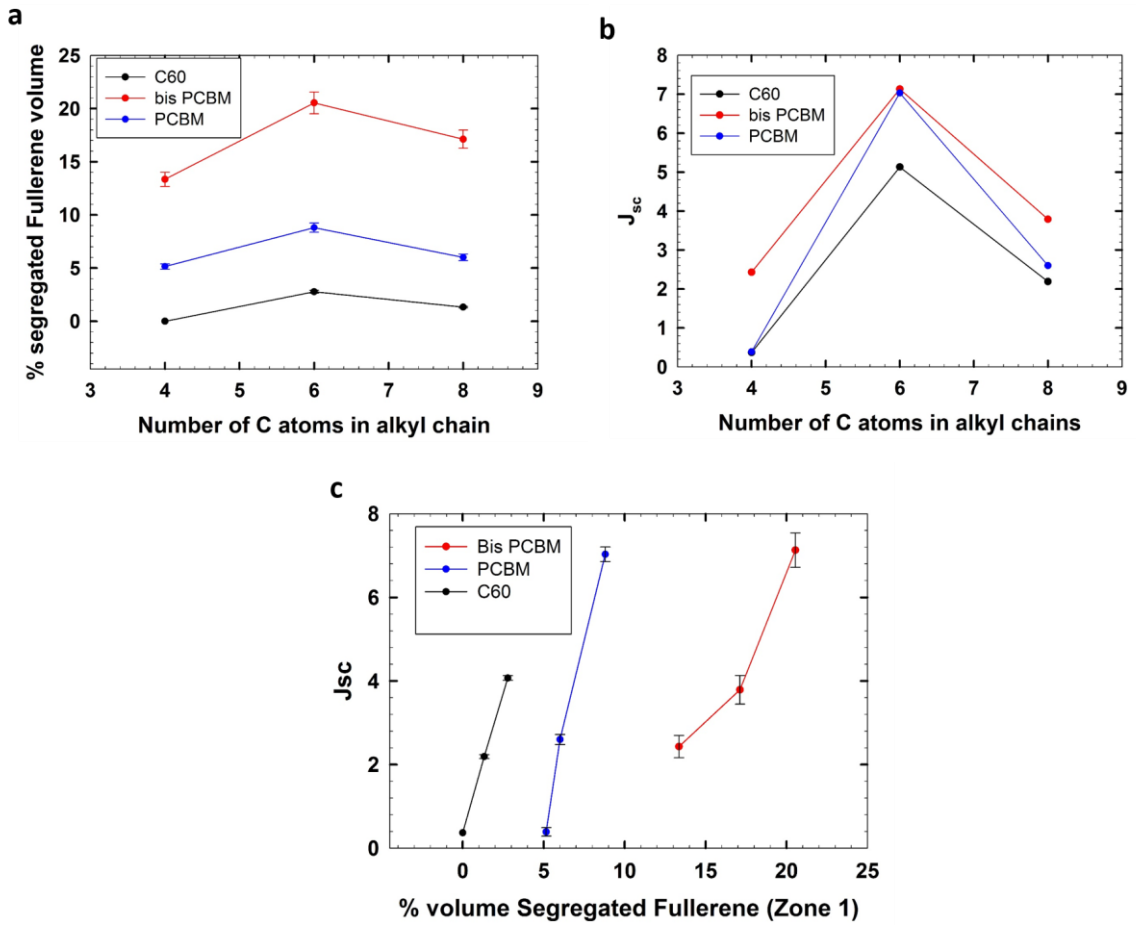

Figure 5 a) Volume of segregated fullerenes in Zone 1 and b) J_{sc}, vs number of Carbon atoms in alkyl chain, c) correlation between segregated volume of fullerene and J_{sc} in the annealed devices

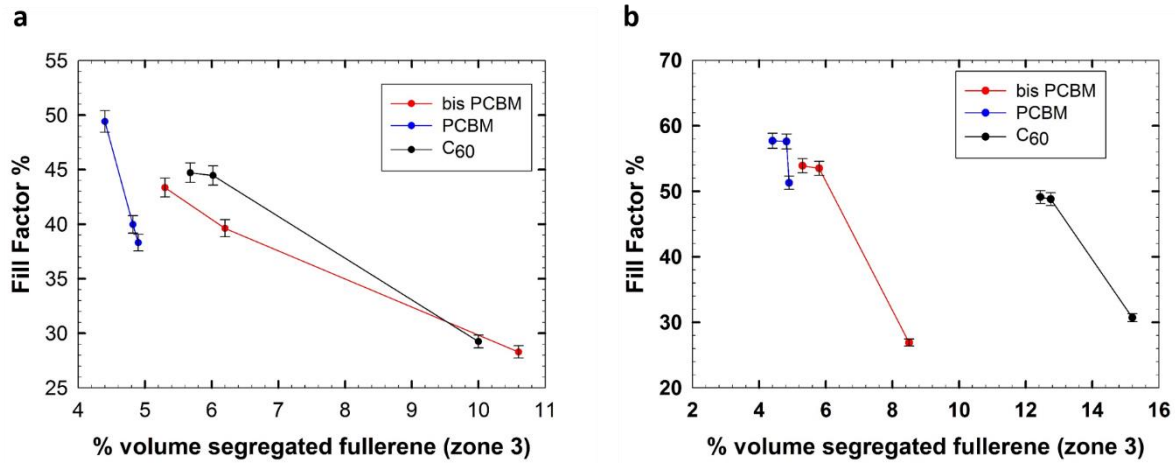

Figure 6 Fill Factor vs segregated volume of fullerene in Zone 3 a) without and b) with Ca layer

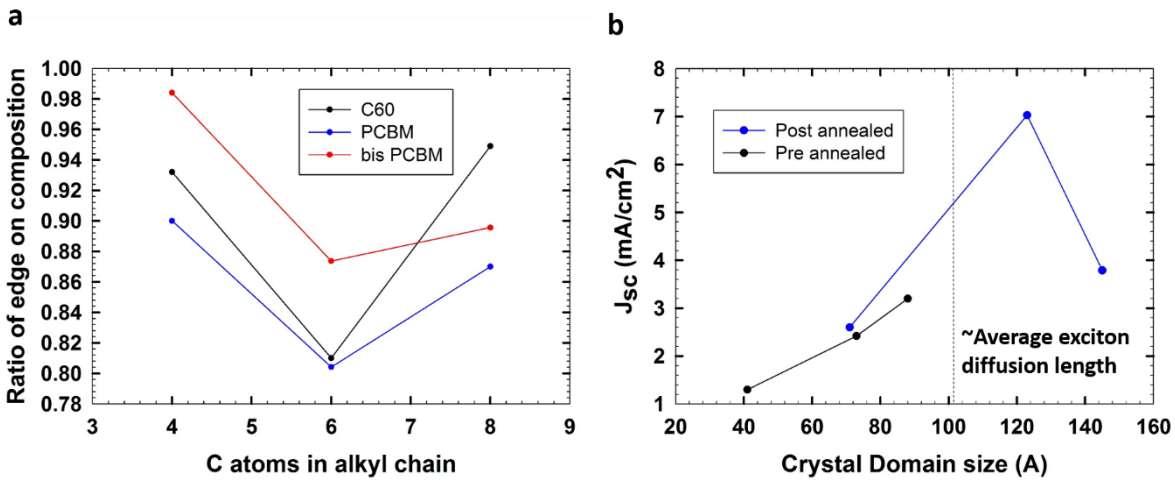

Figure 7. a) Correlation of edge-on to face-on ratio of <100> crystal plane for P3AT-Fullerene samples b) correlation of crystal domain size with J_{sc} for P3AT –PCBM devices

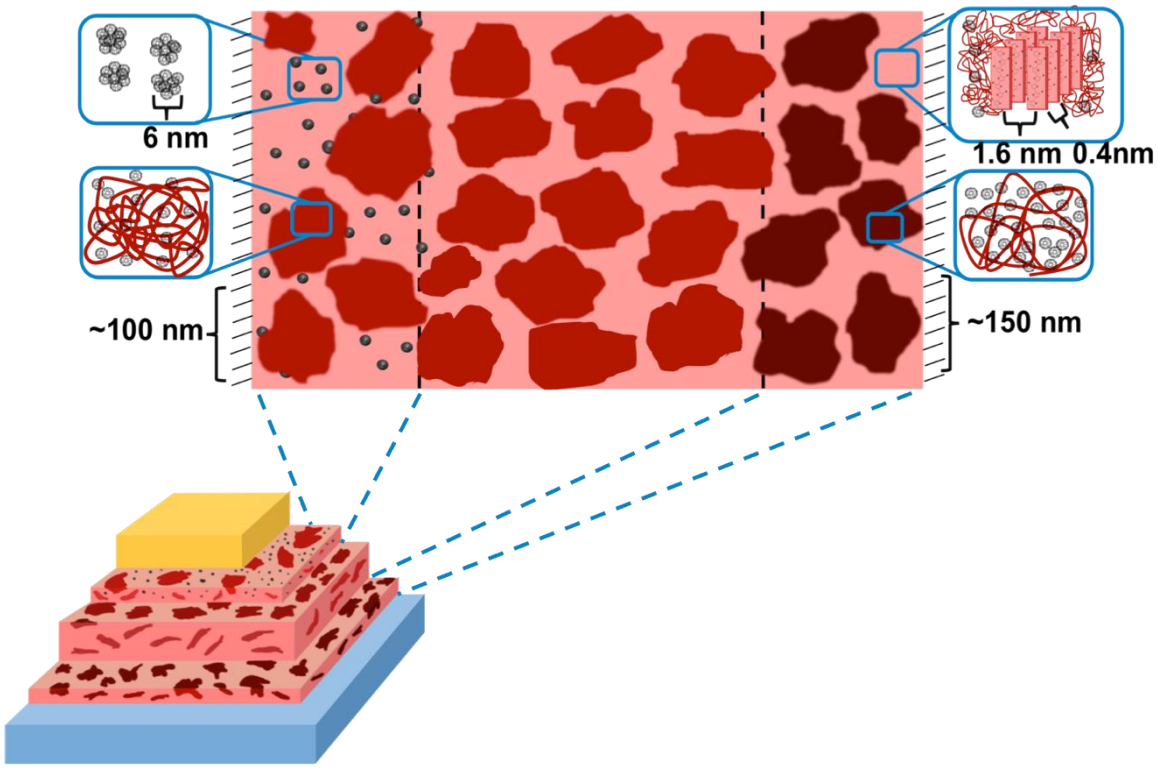

Figure 8. Schematic showing the overall morphological structure of the BHJ

Table 1. Effect of fullerene adlayer on J_{sc} of P3HT-PCBM devices, with and without Ca

	w/o add layer (mA/cm^2)	with add layer (mA/cm^2)
w/o Ca	5.1	5.9
w/ Ca	5.5	7.1